PNAS RESEARCH ARTICLE | CELL BIOLOGY OPEN ACCESS

Microtubule poleward flux as a target for modifying chromosome segregation errors

Patrik Risteski[a,1], Jelena Martinčić[a,1], Mihaela Jagrić[a], Erna Tintor[a], Ana Petelinec[a], and Iva M. Tolić[a,2]

Affiliations are included on p. 11.

Edited by Susanne Lens, Universitair Medisch Centrum Utrecht, Utrecht, Netherlands; received March 13, 2024; accepted October 7, 2024 by Editorial Board Member Rebecca Heald

Cancer cells often display errors in chromosome segregation, some of which result from improper chromosome alignment at the spindle midplane. Chromosome alignment is facilitated by different rates of microtubule poleward flux between sister kinetochore fibers. However, the role of the poleward flux in supporting mitotic fidelity remains unknown. Here, we introduce the hypothesis that the finely tuned poleward flux safeguards against lagging chromosomes and micronuclei at mitotic exit by promoting chromosome alignment in metaphase. We used human untransformed RPE-1 cells depleted of KIF18A/kinesin-8 as a system with reduced mitotic fidelity, which we rescued by three mechanistically independent treatments, comprising low-dose taxol or codepletion of the spindle proteins HAUS8 or NuMA. The rescue of mitotic errors was due to shortening of the excessively long overlaps of antiparallel microtubules, serving as a platform for motor proteins that drive the flux, which in turn slowed down the overly fast flux and improved chromosome alignment. In contrast to the prevailing view, the rescue was not accompanied by reduction of overall microtubule growth rates. Instead, speckle microscopy revealed that the improved chromosome alignment in the rescue treatments was associated with slower growth and flux of kinetochore microtubules. In a similar manner, a low-dose taxol treatment rescued mitotic errors in a high-grade serous ovarian carcinoma cell line OVKATE. Collectively, our results highlight the potential of targeting microtubule poleward flux to modify chromosome instability and provide insight into the mechanism through which low doses of taxol rescue certain mitotic errors in cancer cells.

microtubule poleward flux | chromosome alignment | chromosome segregation | mitosis | chromosome instability

Significance

Cancer cells usually exhibit errors in chromosome segregation, often stemming from inefficient alignment of chromosomes at the mitotic spindle midplane. This alignment relies on chromosome attachment to microtubules, which behave like conveyor belts fluxing toward the spindle pole. We propose a hypothesis that the finely tuned microtubule poleward flux safeguards against mitotic errors by facilitating chromosome alignment. In healthy and cancer cells with overly fast flux, we rescued mitotic errors by slowing down the flux. Thus, by linking the central role of the flux in chromosome alignment with mitotic fidelity, we reveal a mechanism underlying specific mitotic errors. Our findings underscore the potential of targeting microtubule poleward flux to modify chromosomal instability (CIN) in cancer cells.

To achieve proper inheritance of the duplicated genome, the cell aligns chromosomes at the spindle equator before dividing them between the daughter cells. Chromosome alignment at the metaphase plate promotes synchronous poleward movement of chromosomes in anaphase and thus their faithful segregation (1). A precisely formed metaphase plate is critical for the maintenance of genome stability because misaligned chromosomes may lag behind separating chromosome masses or remain near the pole throughout mitosis to form micronuclei (2–6), which are prone to acquiring DNA damage and undergoing chromosomal rearrangements, including chromothripsis (7–9). Therefore, chromosome alignment defects are considered to be one of the origins of chromosomal instability (CIN) in cancer cells (10, 11) and are implicated in the development of oncogene-independent selective advantage (12).

Essential to chromosome alignment on the spindle are microtubules and microtubule-associated proteins, which jointly exert forces on kinetochores and chromosome arms to maintain their position at the spindle equator (13). Regulation of the microtubule growth rates and stability is crucial in the context of chromosome missegregation because excessively fast microtubule growth is a feature of cancer cells that exhibit CIN, and taxol treatment can rescue chromosome missegregation by slowing down microtubule growth (14–16). Microtubule dynamics is modulated by a variety of proteins, with the most prominent player being the motor protein KIF18A/kinesin-8. This protein suppresses polymerization of microtubule plus ends (17, 18), thereby limiting kinetochore movements (19). Recent studies identified aneuploid cancer cells to be particularly sensitive to the depletion or inhibition of KIF18A (4, 5, 20). Interestingly, in CIN tumor cells that exhibit elevated spindle microtubule dynamics, KIF18A depletion can be exploited to reduce their proliferation, by increasing the already elevated microtubule dynamics, which leads to increased chromosome misalignment and therefore CIN and cell death (5). This is in agreement with the sensitization of tumor cells by elevating the frequency of

Author contributions: P.R., J.M., and I.M.T. designed research; P.R., J.M., M.J., and A.P. performed research; P.R., J.M., M.J., and E.T. analyzed data; and P.R., J.M., and I.M.T. wrote the paper.

The authors declare no competing interest.

This article is a PNAS Direct Submission. S.L. is a guest editor invited by the Editorial Board.

[1]P.R. and J.M. contributed equally to this work.

[2]To whom correspondence may be addressed. Email: tolic@irb.hr.

This article contains supporting information online at https://www.pnas.org/lookup/suppl/doi:10.1073/pnas.2405015121/-/DCSupplemental.

Published November 14, 2024.

chromosome missegregation (21, 22), as high rates of missegregation suppress tumor progression (23, 24). Thus, microtubule dynamics and, consequently, chromosome alignment have a direct effect on CIN levels in cancers.

Apart from its role via suppressing microtubule plus-end dynamics, KIF18A is implicated in chromosome alignment on the spindle via overlap length-dependent forces (25, 26). In this model, kinetochore fibers (k-fibers), which are attached end-on to sister kinetochores, are laterally linked by a bundle of nonkinetochore microtubules called the bridging fiber (27–29). Motor proteins within the overlaps between bridging and k-fibers slide the fibers apart (26), thereby generating their movement toward the poles, known as poleward flux (30–33). The flux of longer k-fibers is faster due to their longer overlaps with bridging fibers, resulting in kinetochore movement toward the spindle midplane (Fig. 1*A*, *Scheme*). In contrast, when the overlaps between the bridging and k-fibers are excessively long, as after KIF18A depletion, the coupling between the fibers becomes overly strong and sister k-fibers undergo equally fast flux, leading to inefficient chromosome alignment (26). Thus, chromosome misalignment can be a consequence of altered microtubule poleward flux.

Besides KIF18A, various other microtubule-associated proteins can modify the microtubule poleward flux, including HAUS6/8 (26, 34, 35), NuMA (26, 36, 37), and KIF4A (26, 36). HAUS8 is a subunit of the augmin complex, which promotes microtubule nucleation along the walls of other microtubules (38–40), particularly the nucleation of bridging fibers (35). NuMA serves as a passive cross-linker for parallel microtubules, working in tandem with dynein to tether microtubules toward the spindle poles (41, 42). The coupling between bridging fibers and k-fibers through NuMA promotes the force transmission to k-fibers and therefore k-fiber flux (26, 36). The forces driving flux are also affected by KIF4A, a plus-end directed motor protein that inhibits the growth of nonkinetochore microtubules (18, 25, 43), thereby shortening bridging fiber overlaps and in turn slowing down k-fiber flux (26). In addition to regulating the flux, these proteins have been implicated in chromosome alignment and the occurrence of chromosome segregation errors (1, 3, 26). However, the role of microtubule poleward flux in safeguarding mitotic fidelity is unknown.

Here, we probe the idea that microtubule poleward flux promotes chromosome inheritance fidelity by helping chromosome alignment and explore the potential of targeting flux to reduce mitotic errors. In nontransformed cells, lagging chromosomes and micronuclei induced by KIF18A depletion were partially rescued by a low dose of taxol or codepletion of HAUS8 or NuMA. The treatments that rescued mitotic errors in KIF18A-depleted cells did so by shortening the antiparallel overlaps and slowing down the flux and growth of kinetochore microtubules, thereby improving chromosome alignment, rather than by slowing down microtubule growth in general. Reducing overlaps and flux rates restored chromosome alignment and improved segregation fidelity in an ovarian cancer cell line. These findings highlight the potential to modify CIN in cancer cells by targeting microtubule poleward flux.

Results

Lagging Chromosomes and Micronuclei Caused by Chromosome Misalignment can be Rescued by Slowing Down Microtubule Poleward Flux. This study posits the following hypothesis: Faster poleward flux of spindle microtubules leads to chromosome misalignment in metaphase, which in turn results in lagging chromosomes during anaphase and micronuclei in the following interphase. The primary implication of this hypothesis is that alterations to the microtubule poleward flux have the potential to rescue these mitotic errors.

To explore our hypothesis, we used human nontransformed hTERT-immortalized retinal pigment epithelium cells (RPE-1), which we depleted of KIF18A because this depletion leads to chromosome misalignment (18, 19, 44–47), occurrence of lagging chromosomes and micronuclei (2, 19, 44, 46), and excessively fast poleward flux of k-fibers (26). To test whether lagging chromosomes and micronuclei in this system can be rescued by additional treatments, we used three mechanistically independent approaches: i) we treated KIF18A-depleted cells with a low dose of paclitaxel (taxol), a treatment that partially rescues mitotic errors in cancer cells with increased microtubule dynamics (15, 48); ii) we codepleted HAUS8, a subunit of the augmin complex, because this codepletion rescues chromosome misalignment of KIF18A-depleted cells (26); and iii) we codepleted NuMA, which regulates the poleward flux of k-fibers (26) (Fig. 1*A* and *SI Appendix*, Figs. S1 and S2 *A*–*C*). Remarkably, all three treatments alleviated the increased incidence of both lagging chromosomes and micronuclei induced by the depletion of KIF18A (Fig. 1 *B* and *C*). Moreover, these treatments improved the alignment of chromosomes at the metaphase plate in KIF18A-depleted cells (Fig. 1 *A* and *D* and *SI Appendix*, Fig. S2*D* and Movie S1). As a scenario with increased chromosome misalignment beyond what was observed with KIF18A depletion alone, we used codepletion of kinesin-4/KIF4A and KIF18A (26) and found that this codepletion led to a further increase in the occurrence of lagging chromosomes and micronuclei (Fig. 1 *A*–*D*). Across all conditions, the degree of chromosome misalignment correlated with the incidence of lagging chromosomes and with the occurrence of interphase micronuclei (Fig. 1*E* and *SI Appendix*, Fig. S2*E*). The latter two phenomena showed a similar trend (*SI Appendix*, Fig. S2*F*), in agreement with previous studies linking chromosome segregation errors and micronuclei (3, 49). Overall, our findings suggest that the mitotic errors in KIF18A-depleted cells can be mitigated by improving chromosome alignment on the metaphase spindle.

Given the crucial role of microtubule poleward flux in promoting chromosome alignment on the spindle (13, 26) and in the synchronization of chromosome movements during anaphase (50), we explored whether the observed changes in chromosome missegregation can be explained by the changes in microtubule poleward flux rates. To measure the flux rates, we used the recently developed fluorescence speckle microscopy based on a low concentration (1 nM) of SiR-tubulin (26, 51). The key advantage of this method lies in its ability to measure the poleward flux of individual microtubules, as the movement of individual speckles on the microtubule lattice corresponds to the flux of the microtubule carrying them. However, a potential concern is that SiR-tubulin might influence microtubule dynamics. Nevertheless, despite being taxol-based, SiR-tubulin has been shown to have a reduced impact on tubulin polymerization kinetics (52). Consistent with this, during the brief period when SiR-tubulin was used to visualize speckles, the interkinetochore distance remained unchanged, whereas it decreased upon addition of 2 nM taxol (*SI Appendix*, Fig. S3 *A* and *B*), as expected for low nanomolar taxol doses (53). These data indicate that unlike taxol, SiR-tubulin did not alter microtubule dynamics in our experiments. Using this SiR-tubulin-based method, we measured the flux rates separately for kinetochore and bridging microtubules (*SI Appendix*, Fig. S3 *C* and *D*). Across all conditions, the relationships between the microtubule flux parameters were in agreement with the flux-driven kinetochore centering model (*SI Appendix*, Fig. S3 *E* and *F*) (26). Interestingly, the conditions with k-fiber flux rates faster than those of untreated cells showed an increased

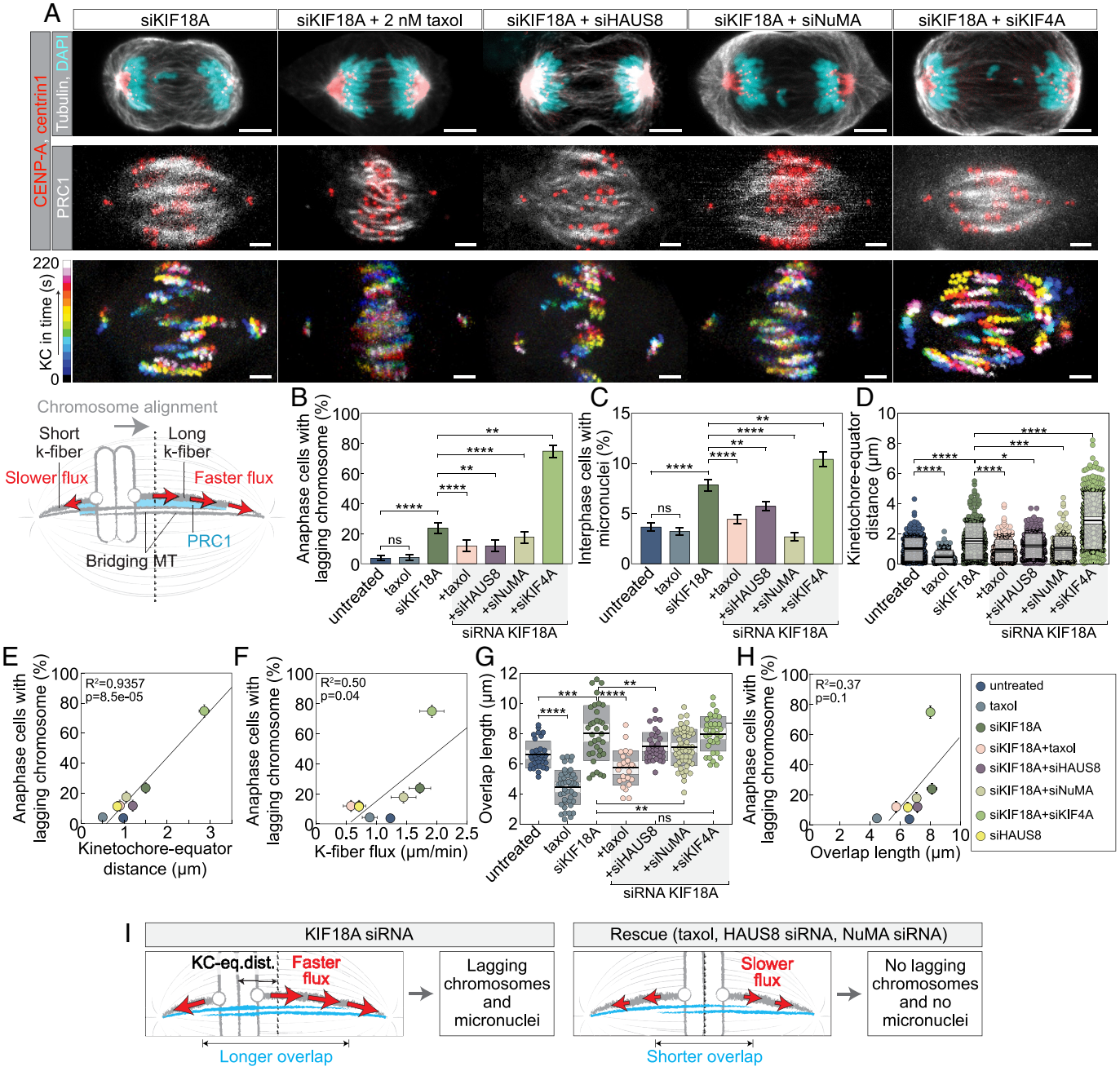

Fig. 1. Lagging chromosomes and micronuclei in KIF18A-depleted cells can be rescued by decelerating microtubule poleward flux. (*A*) RPE-1 cells stably expressing CENP-A-GFP and centrin1-GFP (*Top*, *Middle*: red; *Bottom*: temporal color projection) for each respective treatment. The cells are immunostained for tubulin-AF-594 (*Top*: gray) or PRC1-AF-594 (*Middle*: gray) and dyed with DAPI (*Top*: cyan). Scale bar, 5 μm (*Top*), 2 μm (*Middle* and *Bottom*). Maximum intensity z-projection (*Top* and *Middle*). The scheme depicts the flux-driven centering model. When a kinetochore pair is off-centered, the longer k-fiber exhibits a more extended overlap with the bridging fiber, strengthening the coupling and causing a faster flux compared to the shorter sister k-fiber. Consequently, the kinetochore pair moves in the direction of the longer k-fiber, i.e., toward the spindle midplane. (*B*) Percentage of anaphase cells with lagging chromosomes. Number of analyzed cells for treatments from *Left* to *Right*: 138, 95, 148, 76, 76, 102, 83, and 96. (*C*) Percentage of interphase cells with micronuclei. Number of analyzed cells for treatments from *Left* to *Right*: 2,215, 2,421, 2,269, 2,215, 2,675, 1,676, 1,768, and 2,455. (*D*) Distance between sister kinetochore pair midpoints and the spindle equator. Number of distances measured for sister kinetochore pairs from the equator for treatments from *Left* to *Right*: 258, 97, 198, 190, 242, 191, 235, and 137. (*E*) Percentage of anaphase cells with lagging chromosomes plotted against the kinetochore-equator distance, color-coded for treatments. Without siKIF18A+siKIF4A, $P = 0.03$, $R^2 = 0.60$. (*F*) Percentage of anaphase cells with lagging chromosomes plotted against the k-fiber flux, color-coded for treatments. Without siKIF18A+siKIF4A, the correlation was not significant: $P = 0.19$, $R^2 = 0.30$. (*G*) PRC1-labeled fiber overlap length. Number of PRC1-labeled bundles measured for treatments from *Left* to *Right*: 33, 45, 35, 27, 35, 53, 35, and 30. (*H*) Percentage of anaphase cells with lagging chromosomes plotted against the PRC1-labeled overlap length, color-coded for treatments, see the legend on the *Right*. Without siKIF18A+siKIF4A, $P = 0.05$, $R^2 = 0.56$. (*I*) Schematic showing that increased microtubule poleward flux leads to increased chromosome misalignment on the spindle, which in turn causes higher frequencies of lagging chromosomes in anaphase and micronuclei in the next cell cycle. Kinetochore-equator distances, overlap lengths, and k-fiber flux for untreated, siKIF18A, siKIF18A+siHAUS8, siKIF18A+siKIF4A, and siHAUS8 were replotted from (26). Statistical tests: two-proportions z-test (*B* and *C*), Mann–Whitney test (*D*), *t* test (*G*). *P* = *P*-value, R^2 = coefficient of determination. *P*(ns) > 0.05, **P* = 0.01 to 0.05, ***P* = 0.01 to 0.001, ****P* = 0.001 to 0.0001, *****P* < 0.0001.

incidence of lagging chromosomes (Fig. 1*F* and *SI Appendix*, Fig. S3*G*), suggesting that flux perturbations affect chromosome inheritance fidelity.

As the increased microtubule poleward flux in KIF18A-depleted cells was proposed to be a result of extended overlaps between the antiparallel microtubules and thus higher sliding forces (25, 26),

we set out to determine the size of these overlaps in treatments that rescued mitotic errors. We found that the antiparallel overlap length, measured as the length of stripes decorated by the cross-linker of antiparallel microtubules PRC1 (27, 54), was reduced in KIF18A-depleted cells after the low-dose taxol treatment or after codepletion with HAUS8 or NuMA (Fig. 1 *A* and *G* and *SI Appendix*, Fig. S2*C*). These results indicate that the extended antiparallel overlaps play a role in generating mitotic errors in KIF18A-depleted cells. The lack of significant changes in overlap length and microtubule poleward flux under KIF4A and KIF18A codepletion condition with respect to KIF18A depletion alone (Fig. 1*G* and *SI Appendix*, Fig. S3*C*) suggests that other mechanisms may be contributing to the mitotic defects in the KIF4A and KIF18A codepletion. Across all conditions, overlaps longer than in untreated cells tended to coincide with faster poleward flux, worse chromosome alignment, and a greater prevalence of lagging chromosomes and micronuclei (Fig. 1*H* and *SI Appendix*, Fig. S3 *H–J*).

Taken together, our results suggest that overlap length-dependent microtubule poleward flux safeguards mitotic fidelity by promoting chromosome alignment. It is important to acknowledge that in principle, each specific treatment applied here could have influenced mitotic fidelity independently of the overlap length and poleward flux. Nonetheless, the fact that three mechanistically independent approaches rescued both the flux-dependent chromosome alignment and segregation errors supports the causal connection between microtubule poleward flux and mitotic fidelity (Fig. 1*I*).

Altered Overall Growth Rates of Microtubules cannot Explain the Changes in Chromosome Alignment and Missegregation. Aberrant microtubule dynamics and stability are features of cancer cells that lead to CIN, and taxol treatment can rescue chromosome missegregation by reducing excessive microtubule growth velocities (14–16). However, it is unclear how the treatments that affect microtubule dynamics, including taxol and our codepletions, rescue mitotic errors. There are two main possibilities: First, the primary mechanism of action may involve a reduction in the growth rate of all microtubules. In this scenario, treatments with a more pronounced slowdown of overall microtubule growth should more efficiently rescue mitotic errors. Second, the rescue treatments may influence mitotic fidelity by decreasing the plus-end growth rate of kinetochore microtubules. This rate depends not only on intrinsic microtubule growth but also on the forces exerted by the kinetochore onto the microtubule plus ends. These forces, in turn, are dependent on the microtubule poleward flux. In this scenario, treatments with a more pronounced slowdown of the poleward flux and of the kinetochore microtubule growth velocity should more efficiently rescue the errors.

To distinguish between these possibilities, we first measured the growth velocities of microtubules in bipolar spindles as indicators of the overall microtubule growth in each condition. For this purpose, we tracked spots of GFP-labeled EB3, which marks the plus ends of growing microtubules (Fig. 2*A* and *SI Appendix*, Fig. S4 *A* and *B* and Movie S2) (55). We measured the velocity of the EB3 spots that moved from the centrosome toward the cell periphery, which we interpret as astral microtubules, and of the EB3 spots that terminated at chromosomes, which we interpret as microtubules within k-fibers, though this group may contain also other spindle microtubules. Taxol decreased EB3 spot velocities on astral and k-fiber microtubules in wild-type cells (14), whereas KIF18A depletion had no effect (Fig. 2*B*) (18). Interestingly, the treatments that rescued mitotic errors in KIF18A-depleted cells either did not change (taxol) or increased the EB3 spot velocities (HAUS8 or NuMA codepletion) (Fig. 2*B*). Across conditions, the EB3 spot velocity was not predictive of the efficiency of chromosome alignment (Fig. 2*C*). All the results were consistent between astral and k-fiber microtubules, indicating that the growth velocities of free (unattached) microtubule plus ends are similar inside and outside of the spindle. Taken together, these findings are not consistent with the hypothesis that a general perturbation of the microtubule plus-end dynamics underlies the improved chromosome alignment and mitotic fidelity following taxol treatment, as well as after codepletion of HAUS8 or NuMA, in KIF18A-depleted cells.

Altered Kinetochore Microtubule Growth and Flux can Explain the Changes in Chromosome Alignment and Missegregation. To explore the hypothesis that taxol and HAUS8 or NuMA codepletions in KIF18A-depleted cells influence mitotic fidelity by decreasing the plus-end growth rate of k-fibers, we used speckle microscopy to measure growth or shrinkage rates of kinetochore microtubules at their plus end, i.e., at the kinetochore (Fig. 3*A*). Given that pairs of sister kinetochores oscillate around the spindle midplane during metaphase (19, 56–58), we assessed microtubule dynamics separately at the leading and the trailing kinetochore, where the leading kinetochore refers to the one moving toward its associated pole, while the trailing kinetochore is the one moving away from its linked pole. We measured the velocity with which a speckle, fixed on the lattice of a kinetochore microtubule, moves with respect to its kinetochore (Fig. 3*A*). If the speckle moves away from the kinetochore, we interpret this as growth of the kinetochore microtubule. Conversely, if the speckle moves toward the kinetochore, we consider it as shrinkage of the kinetochore microtubule.

We found that the trailing kinetochore microtubules grew at the plus end under all examined conditions (Fig. 3*B*). Taxol treatment reduced their growth rate, whereas KIF18A depletion increased it. Furthermore, taxol treatment and HAUS8 codepletion decreased the excessively high kinetochore microtubule growth rate of KIF18A-depleted cells. Codepletion of NuMA caused slightly slower growth, though the effect was not significant (Fig. 3*B*).

In contrast to the trailing kinetochore microtubules, their leading counterparts showed slow growth at the plus end, which was similar across all treatments (Fig. 3*C*). This result suggests that the leading kinetochore microtubules are typically in a state of slow growth or pausing at their plus end and that the used treatments did not affect their plus-end dynamics. It is worth noting that the results for speckles on the leading kinetochore microtubules might be biased toward higher microtubule growth velocities because speckles that disappeared within the first 30 s after appearance, due to depolymerization of the leading microtubule plus end, were too short-lived to be analyzed. However, such disappearance events were rare, suggesting that the bias was not substantial. As the measurements of the trailing microtubule growth velocities were unbiased, because these speckles moved away from their kinetochore, and were more abundant, we use them as representative of kinetochore microtubule plus-end growth in the subsequent analysis.

Across conditions, kinetochore microtubule plus-end growth velocity strongly correlated with the k-fiber flux velocity (Fig. 3*D*), but did not correlate with EB3 spot velocity (Fig. 3*E*). These results indicate that the changes in the kinetochore microtubule plus-end growth are mainly determined by the altered forces acting at and near the kinetochore, rather than by the altered intrinsic growth of free plus ends in each condition.

The velocity of kinetochore movements correlated with the k-fiber flux and the kinetochore microtubule plus-end growth

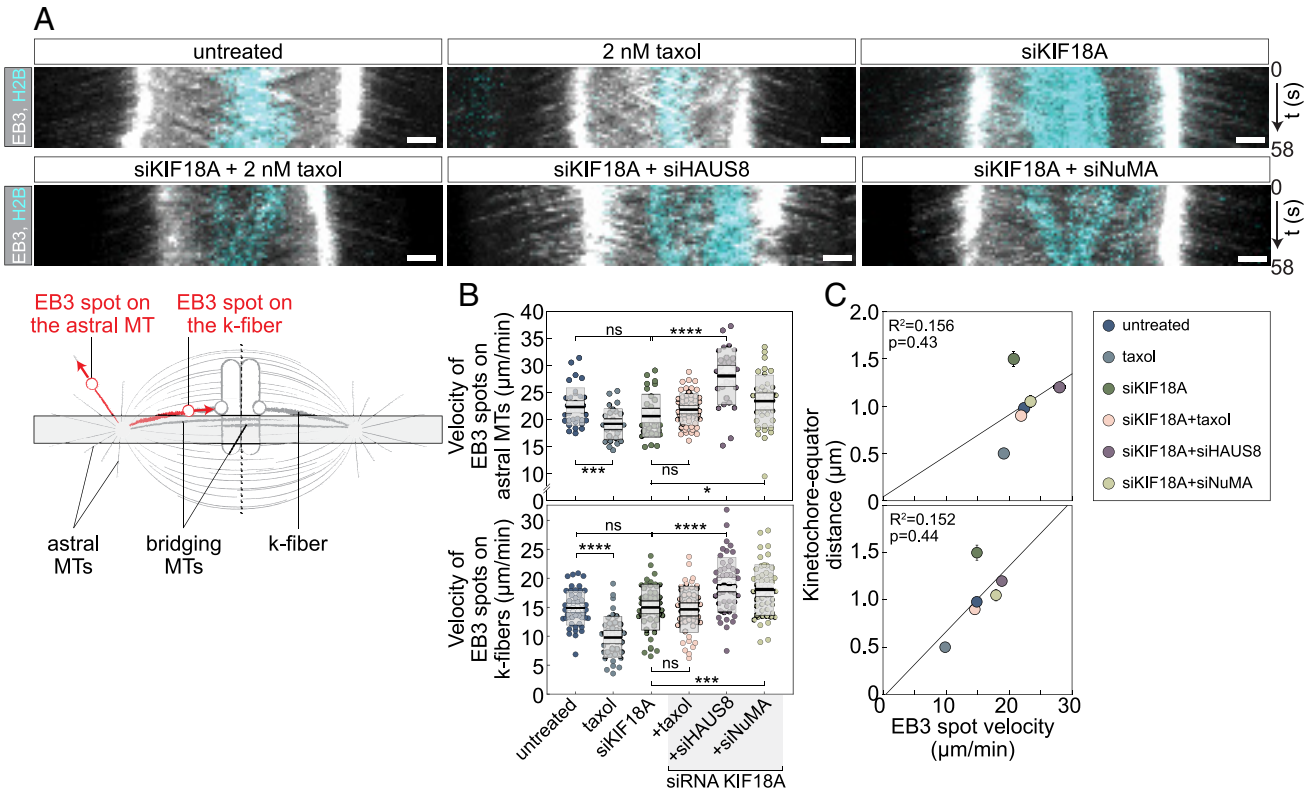

Fig. 2. Treatments that reduce microtubule poleward flux do not reduce astral microtubule plus-end dynamics. (*A*) Kymographs (temporal projections) of RPE-1 cells with stable expression of EB3-GFP (gray) and H2B-mCherry (cyan), per corresponding treatment. (Scale bar, 2 μm.) The scheme indicates the position at which the kymographs were created and where EB3 spots on astral and kinetochore microtubules were tracked. (*B*) EB3 spot velocity, measured on astral (*Top*) or kinetochore (*Bottom*) microtubules of metaphase spindles. Number of EB3 spots on astral microtubules measured for treatments from *Left* to *Right*: 35, 28, 31, 57, 29, and 38. Number of EB3 spots on kinetochore microtubules measured for treatments from *Left* to *Right*: 51, 40, 50, 50, 50, and 50. (*C*) Kinetochore-equator distance plotted against the EB3 spot velocity for astral (*Top*) and kinetochore (*Bottom*) microtubules, color-coded for treatments. Legend is at the *Bottom right* corner. Kinetochore-equator distances for untreated, siKIF18A, siKIF18A + siHAUS8, and siKIF18A+siKIF4A were replotted from (26). Statistical tests: *t* test (B). *P*-value as in Fig. 1.

velocity across treatments (Fig. 3 *F* and *G* and *SI Appendix*, Fig. S5*A*). Interestingly, we found that treatments with increased kinetochore velocities, as well as those with increased kinetochore microtubule plus-end growth velocities, tend to have worse chromosome alignment (Fig. 3 *H* and *I*). This is in contrast with the absence of a correlation between EB3 spot velocity and the efficiency of chromosome alignment (Fig. 2*C*). We propose that a faster poleward flux is accompanied by a faster growth of the kinetochore microtubule plus end, allowing for faster kinetochore movements during their oscillations around the spindle midplane, ultimately resulting in a broader metaphase plate (Fig. 3*J*). Thus, altered poleward flux of kinetochore microtubules due to changes in the antiparallel overlaps, rather than a general perturbation of the microtubule plus-end dynamics, can explain the improved chromosome alignment and mitotic fidelity following taxol treatment, as well as after codepletion of HAUS8 or NuMA, in KIF18A-depleted cells.

Chromosome Missegregation Rates in the OVKATE Cancer Cell Line can be Reduced by Altering Microtubule Poleward Flux. To investigate the relevance of our findings on the protective role of microtubule poleward flux in maintaining mitotic fidelity for cancer cells, we set out to rescue mitotic errors by using a low-dose taxol treatment in specific cancer cell lines. To find promising candidate lines, we performed a mini screen where we roughly assessed the presence of wider metaphase plates and longer spindles, using the latter as an indicator of extended antiparallel overlaps. We tested the following lines: rhabdomyosarcoma (RD), colorectal adenocarcinoma (DLD-1), lung adenocarcinoma (A549), and ovarian carcinoma (OVKATE and OVSAHO) (*SI Appendix*, Fig. S6 *A* and *B*). OVKATE was identified as the most promising candidate, prompting us to select it along with its counterpart, OVSAHO, both serving as models of high-grade serous ovarian carcinoma (59, 60).

We aimed to assess whether targeting microtubule poleward flux could reduce chromosome segregation errors in OVKATE and OVSAHO cells. We found that a low-dose taxol treatment decreased the occurrence of lagging chromosomes in OVKATE cells, whereas in OVSAHO cells this decrease was smaller and not significant (Fig. 4*A* and *SI Appendix*, Fig. S6 *B* and *C*; our result in OVSAHO differs from a previous study (15), which found a significant reduction of anaphase errors). In line with fewer lagging chromosomes, OVKATE cells also had fewer micronuclei after taxol treatment (Fig. 4*B*). In contrast to OVKATE, the number of micronuclei in OVSAHO cells increased after taxol treatment (Fig. 4*B*), possibly due to the stabilization of BRCA2-driven uncongressed chromosomes and premature chromosome segregation in this cell line (15, 61, 62), which can cause the formation of micronuclei (61, 62).

To assess whether the difference in the taxol effect on mitotic fidelity between the two cancer cell lines can be explained by our model, we tested the model's predictions for these cases. The model suggests that taxol affects chromosome alignment, microtubule poleward flux, and antiparallel microtubule overlaps in OVKATE, but to a lesser extent or not at all in OVSAHO cells. Indeed, we found that taxol treatment improved chromosome

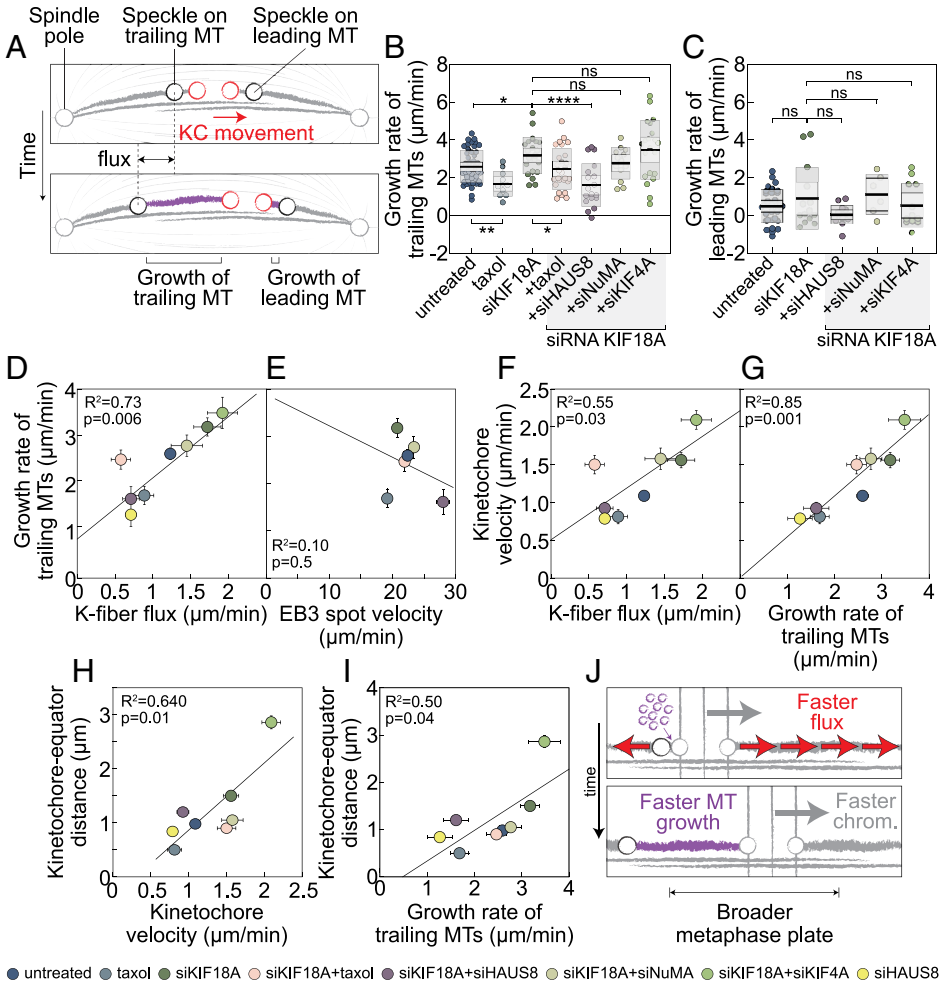

Fig. 3. Altered microtubule poleward flux affects the metaphase plate width and kinetochore velocities via its effect on k-fiber growth rates. (*A*) Schematic depiction illustrating the differentiation between leading and trailing kinetochores, along with their respective associated k-fibers and bridging fibers. (*B*) Growth rate of microtubules measured as speckle-to-kinetochore velocity on k-fiber associated with trailing kinetochore. Number of analyzed k-fiber speckles associated with trailing kinetochores for treatments from *Left* to *Right*: 48, 11, 24, 27, 18, 13, 21, and 14. (*C*) Growth rate of microtubules measured as speckle-to-kinetochore velocity on k-fiber associated with leading kinetochore. Number of analyzed k-fiber speckles associated with leading kinetochores for treatments from *Left* to *Right*: 32, 14, 14, 6, 12, and 16. (*D*) Growth rate of microtubules associated with trailing kinetochore plotted against the k-fiber flux rate, color-coded for treatments. (*E*) Growth rate of microtubules associated with trailing kinetochore plotted against the EB3 spot velocity, color-coded for treatments. (*F*) Kinetochore velocity plotted against the k-fiber flux rate, color-coded for treatments. (*G*) Kinetochore velocity plotted against the growth rate of microtubules associated with trailing kinetochore, color-coded for treatments. (*H*) Kinetochore-equator distance plotted against the kinetochore velocity, color-coded for treatments. (*I*) Kinetochore-equator distance plotted against the growth rate of microtubules associated with trailing kinetochore, color-coded for treatments. (*J*) Schematic showing that microtubule poleward flux leads to microtubule growth at the plus-ends of k-fibers associated with trailing kinetochores and in turn kinetochore movement within the metaphase plate. Note that kinetochore-equator distances and k-fiber flux rates for untreated, siKIF18A, siKIF18A+siHAUS8, siKIF18A+siKIF4A, and siHAUS8 were replotted from (26). Statistical tests: *t* test (*B* and *C*). *P*-value as in Fig. 1.

alignment in OVKATE cells, whereas the improvement was smaller and not significant in OVSAHO cells (Fig. 4*C* and *SI Appendix*, Fig. S6*D*). Similarly, taxol decreased the microtubule poleward flux velocity in OVKATE cells, while the change was again smaller and not significant in OVSAHO cells (Fig. 4*D* and Movie S3). Finally, we found that the origin of the differential effect of taxol treatment on microtubule poleward flux lies in the differential effect on overlap length, as overlaps were shortened by taxol in OVKATE cells, but not in OVSAHO cells (Fig. 4*E* and *SI Appendix*, Fig. S6 *E* and *F*). Furthermore, the overlaps in untreated OVSAHO cells were shorter compared to those in OVKATE cells (Fig. 4*E*), implying that the initial overlap lengths may serve as an indicator of whether chromosome misalignment and missegregation can be rescued by reducing microtubule poleward flux.

To explore whether the observed differences between the two cell lines may be due to their different expression of KIF18A, we examined the KIF18A copy number and expression levels across a cell line database using DepMap (63, 64). Indeed, this analysis revealed that the OVKATE cell line exhibits markedly lower expression of KIF18A than OVSAHO, and the lowest among the lines examined here (Fig. 4*F*). This low expression of KIF18A may explain the longer antiparallel microtubule overlaps and the observed taxol-induced rescue in these cells.

Collectively, our results show that by modifying the length of antiparallel overlaps, which serve as a platform for motor proteins that drive microtubule poleward flux, chromosome missegregation rates can be altered in certain cancer cells. We propose that the difference in the effect of taxol between the two ovarian cancer cell lines is due to the fact that OVKATE cells possess lengthy antiparallel overlaps that can be shortened by taxol, leading to a slower microtubule poleward flux, rescuing chromosome alignment and segregation fidelity. Conversely, OVSAHO cells have short overlaps that remain unchanged after taxol treatment, lacking downstream

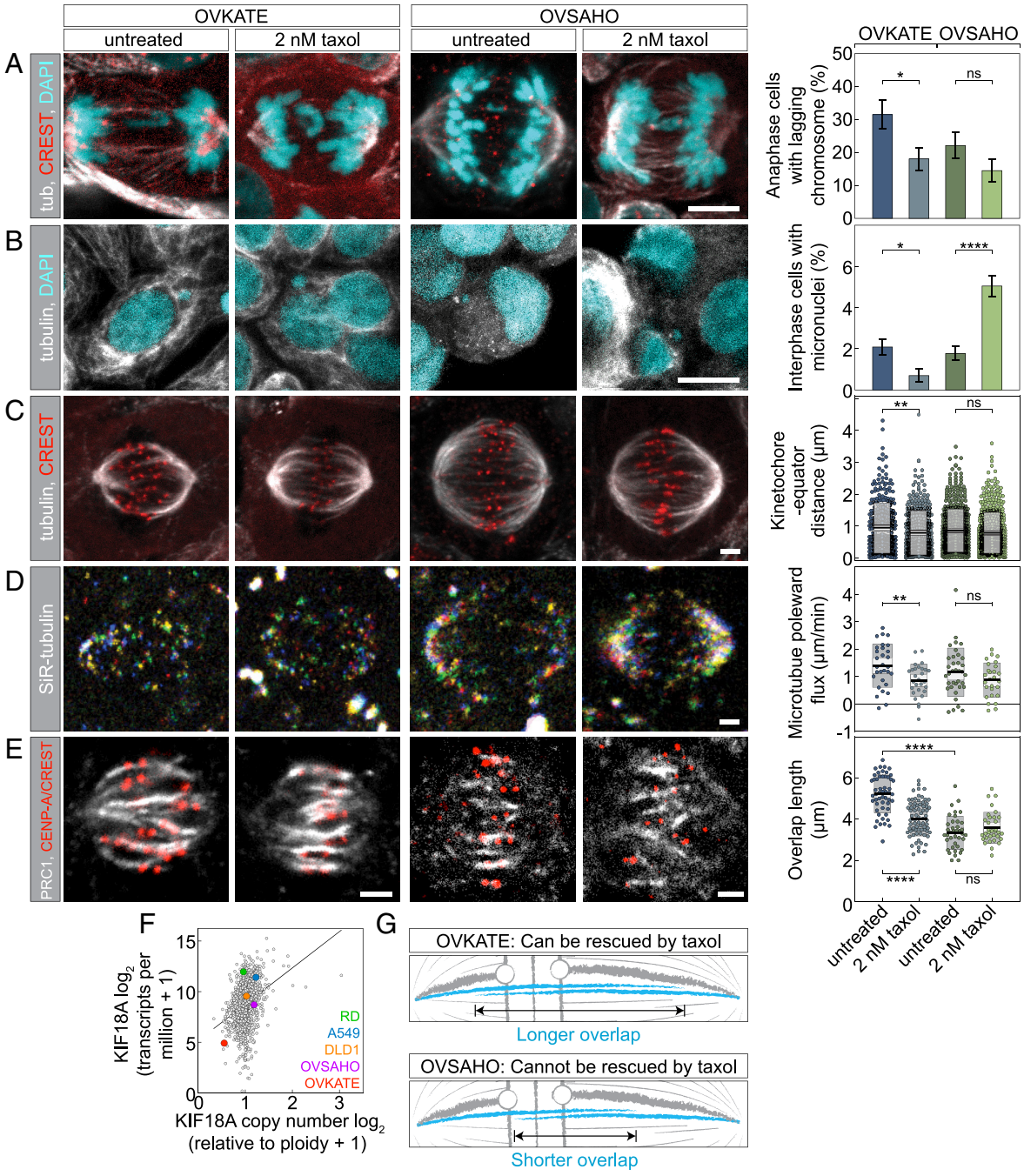

Fig. 4. Modulation of chromosome missegregation rates by targeting microtubule poleward flux in ovarian cancer cells. (*A*) OVKATE (*Left*) and OVSAHO (*Right*) cells immunostained for tubulin (gray), CREST (red), and dyed with DAPI (cyan). Untreated (*Left*) and taxol-treated (*Right*) cells are shown. The graph shows the percentage of anaphase cells with lagging chromosome. Number of analyzed cells for treatments from *Left* to *Right*: 100, 103, 96, and 88. (Scale bar, 5 μm.) (*B*) OVKATE (*Left*) and OVSAHO (*Right*) cells immunostained for tubulin (gray) and DAPI (cyan). Untreated (*Left*) and taxol-treated (*Right*) cells are shown. The graph shows the percentage of interphase cells with micronuclei. Number of analyzed cells for treatments from *Left* to *Right*: 1390, 716, 1527, and 1961. (Scale bar, 10 μm.) (*C*) OVKATE (*Left*) and OVSAHO (*Right*) cells immunostained for tubulin (gray) and CREST (red). Untreated (*Left*) and taxol-treated (*right*) cells are shown. The graph shows kinetochore-equator distance. Number of distances between sister kinetochore pairs and the equator measured for treatments from *Left* to *Right*: 337, 365, 507, and 490. (Scale bar, 2 μm.) (*D*) OVKATE (Left) and OVSAHO (*Right*) cells stained with SiR-tubulin. Untreated (*Left*) and taxol-treated (*Right*) cells are shown. Temporal projection of SiR-tubulin speckles. The graph shows microtubule poleward flux rates. Number of SiR-tubulin speckles tracked for treatments from *Left* to *Right*: 30, 28, 36, and 27. (Scale bar, 2 μm.) (*E*) OVKATE (*Left*) and OVSAHO (*Right*) cells immunostained for PRC1 (gray) and CENP-A in OVKATE (red) or CREST in OVSAHO (red). Untreated (*Left*) and taxol-treated (*Right*) cells are shown. The graph shows overlap length. Number of PRC1-labeled bundles measured for treatments from *Left* to *Right*: 53, 74, 39, and 33. (Scale bar, 2 μm). (*F*) Normalized KIF18A gene expression with respect to KIF18A copy number relative to ploidy in cancer cell lines retrieved from DepMap. The cell lines tested here are highlighted by colors, see legend. (*G*) Schematic illustrating that taxol treatment can reduce increased microtubule poleward flux and its adverse effects when overlap lengths are extended. Maximum intensity z-projection (*A*–*C*), single z (*E*). Statistical tests: two-proportions z-test (*A* and *B*), Mann–Whitney test (*C*), *t* test (*D* and *E*). *P*-value as in Fig. 1.

mitotic effects and rescue. Thus, the inherent variations in spindle architecture between OVKATE and OVSAHO cells, especially in microtubule overlaps which are likely influenced by different levels of KIF18A, determine the efficacy of rescuing mitotic errors through the modulation of poleward flux (Fig. 4*G*).

Discussion

In this paper, we show that overlap length-dependent microtubule poleward flux controls chromosome segregation error and micronuclei formation frequencies via its effect on chromosome

alignment (Fig. 5). Specifically, in two systems characterized by excessively long overlaps of antiparallel microtubules, KIF18A-depleted RPE1 cells and the ovarian cancer OVKATE cells, lagging chromosomes and micronuclei were rescued by treatments that shortened the overlaps and slowed down the poleward flux. We propose the following mechanistic explanation for these rescues. When the overlap zones of antiparallel microtubules are shortened, the poleward flux of k-fibers is slower as a result of shorter overlaps between the antiparallel segments of bridging and k-fibers, which serve as a platform for motor proteins that slide these fibers apart and generate poleward flux of k-fibers (26). Slower k-fiber flux relative to bridging fiber flux allows the sister k-fibers to flux at different velocities, which is essential for efficient flux-driven chromosome alignment (26). The alignment occurs because the longer k-fiber wins the tug-of-war against the shorter one and fluxes faster, resulting in the movement of the chromosome toward the spindle midplane.

In addition to the k-fiber flux rate, the polymerization rate at the k-fiber plus end also plays an important role in chromosome alignment. This polymerization rate depends not only on intrinsic microtubule polymerization but also on the forces exerted by the kinetochore onto the k-fiber plus end, which depend on the k-fiber flux. The polymerization rate at the k-fiber plus ends, measured by using speckles, differs from EB3-based microtubule growth measurements because EB3 reflects global polymerization dynamics across all microtubules, whereas speckle microscopy provides more localized insights into microtubule dynamics at k-fiber tips. Thus, speckle microscopy can detect changes resulting from the altered mechanical environment at the kinetochore or variations in forces transmitted through the microtubules, rather than changes in the intrinsic growth rate of microtubule ends. The k-fiber flux and the polymerization rates at the k-fiber plus ends are interdependent, and their net values must be equal for the spindle to maintain a steady-state length. Notably, whereas the flux rate is roughly constant when kinetochores are aligned at the metaphase plate, the plus-end polymerization rates increase and decrease substantially as the kinetochores move within the plate. Our results show that during kinetochore oscillatory movements, in conditions with slower k-fiber flux, the polymerization at the plus end of the trailing k-fiber is slower and the kinetochore movement is slower, producing less extensive oscillations and a tighter metaphase plate. We propose that both effects—the slower plus-end polymerization and the slower flux due to shorter overlaps—promote chromosome alignment in our rescue treatments. Yet, as HAUS8 and NuMA are not plus-end proteins, but localize along spindle microtubules, their depletion likely rescues chromosome alignment by regulating microtubule–microtubule interactions and overlaps, thereby altering plus-end polymerization through biomechanical coupling, rather than directly affecting the k-fiber plus ends.

Microtubule poleward flux is controlled not only by the antiparallel overlaps but also at the spindle pole. The finding that the pole-localized proteins WDR62 and katanin promote synchronous chromosome movement in anaphase (65) highlights the role of the poleward flux in controlling mitotic fidelity. However, as flux rates differ across species and cell types, the functional significance of flux may vary depending on the cell system (66). For instance, spindle microtubules in yeast cells do not undergo poleward flux (67, 68), yet these spindles achieve efficient chromosome congression and maintain high mitotic fidelity. In these cells, kinesin-5 and kinesin-8 motors regulate kinetochore microtubule plus-end dynamics and pulling forces (69–71), which may suffice for proper chromosome congression on small spindles, but not on larger spindles with complex architecture and microtubule distributions.

Previous studies have demonstrated that CIN in colorectal and high-grade serous ovarian cancer cells can be decreased by attenuating the increased microtubule dynamics in these cells by using a low doses of taxol (14, 15). Interestingly, in our KIF18A-depleted cells, a low-dose taxol also decreased CIN, but did not affect the overall microtubule dynamics, inferred from the EB3-based growth rates of astral and k-fiber microtubules on metaphase spindles. Yet, taxol treatment decreased the growth rate of k-fibers at the plus end and their poleward flux velocities. Thus, we propose that a low-dose taxol treatment reduces mitotic errors by affecting the dynamics and flux of k-fibers rather than by changing the general dynamics of microtubules in systems characterized by excessively fast k-fiber flux, such as KIF18A-depleted cells and OVKATE. It is possible that reduced flux rates contribute to the taxol-induced reduction of CIN in other cancer cell lines as well. However, further experiments are needed to explore this possibility.

Overexpression of KIF18A was detected in whole-genome duplicated tumors (5), which could help tumor proliferation by avoiding micronuclei formation via dampened chromosome movements during metaphase. Cancer cell lines with dampened chromosome movements within the metaphase plate, e.g., HeLa—cervical adenocarcinoma (72) and U2OS—osteosarcoma (36, 73) exhibit reduced microtubule poleward flux when compared to nontransformed RPE-1—retinal pigment epithelium cells (26, 74). This is in agreement with our model, where slower flux results in better chromosome alignment. In spite of a tight metaphase plate in these cancer cells, lagging chromosomes may appear as a consequence of inefficient error correction of kinetochore-microtubule attachments due to attenuated kinetochore oscillations (75). However, as most cancer cell lines are transcriptionally distinct from their primary cancer types (76), it would be interesting to study the relationship

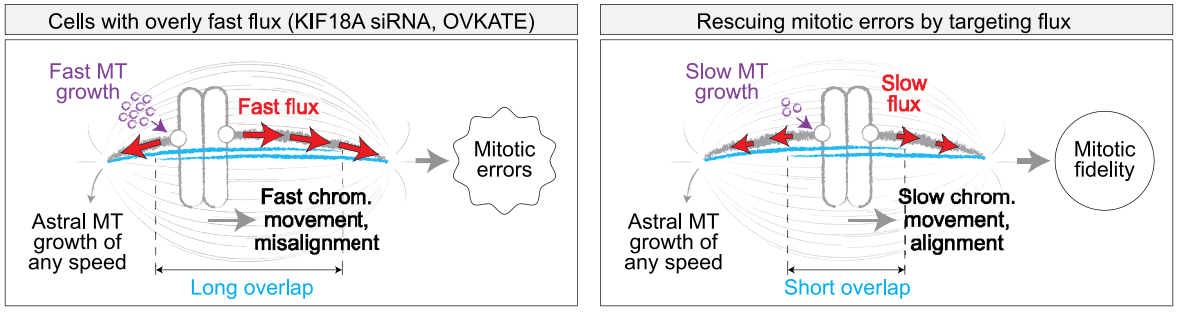

Fig. 5. Enhancing mitotic fidelity by fine-tuning chromosome alignment through microtubule flux. In systems characterized by compromised mitotic fidelity, chromosome segregation errors may be mitigated through targeting elevated microtubule poleward flux caused by overly extended antiparallel microtubules. By shortening these overlap regions, where flux-driving forces are generated, excessive flux and, in turn, kinetochore microtubule growth are slowed down, ultimately leading to improved chromosome alignment on the spindle and fewer lagging chromosomes.

between microtubule flux, chromosome alignment, and mitotic errors in patient tumor samples across various cancer types.

KIF18A promotes normal cell growth and viability as generation of micronuclei due to the lack of KIF18A hampers proliferation through a p53-dependent mechanism (2, 3, 77, 78). In agreement with these studies, we found that the majority of lagging chromosomes which arise due to chromosome alignment defects are able to integrate into the main nucleus, thus decreasing the frequency of micronuclei occurrence with respect to the occurrence of lagging chromosomes. In instances where micronuclei do form, the probability of micronuclei rupture may be a detrimental factor for cell proliferation. As the micronuclear envelope stability depends on chromosome length and gene density (79), it would be interesting to test whether these micronuclei show bias toward certain chromosomes (80). Micronuclei resulting from chromosome misalignment form more stable nuclear envelopes than those resulting from defective kinetochore-microtubule attachments (78). Unlike in normal tissues, micronuclear envelope integrity associated with insufficient KIF18A is compromised in tumors (78). These factors underlying micronuclear integrity might influence cell proliferation following the modification of poleward flux.

By targeting microtubule poleward flux, chromosome alignment is affected independently of kinetochore attachment status (2, 26), and chromosome missegregation rates can be reduced in cells that have increased overlap lengths and microtubule poleward flux velocities. This suggests that microtubule poleward flux could be used as a target to mitigate or aggravate mitotic errors in cancers that show wider metaphase plates and longer spindles, where the latter serves as an indication of extended overlaps and increased microtubule poleward flux. Specifically, by increasing already elevated chromosome misalignment via targeting microtubule poleward flux, e.g., by affecting KIF18A, we speculate that it may be possible to increase the rate of chromosome missegregation beyond the tolerable threshold and promote cancer cell death (21, 22, 81). With the recent development of small-molecule inhibitors targeting KIF18A and their encouraging preclinical efficacy observed in certain human cancer models (82, 83), our study suggests that the misalignment of chromosomes together with elongation of antiparallel overlaps and spindles in cancer cells compared to their noncancer counterparts may signal vulnerability to KIF18A inhibition. These biophysical markers could serve as a basis for developing synthetic lethality strategies that include KIF18A inhibition, aiming to selectively eliminate cells exhibiting elevated microtubule poleward flux.

Materials and Methods

Cell Culture. The hTERT-RPE-1 cell line with stable expression of CENP-A-GFP and centrin1-GFP was a gift from Alexey Khodjakov (Wadsworth Center, New York State Department of Health, Albany, NY). The hTERT-RPE-1 cell line expressing EB3-GFP and H2B-mCherry was a gift from Patrick Meraldi (University of Geneva, Geneva, Switzerland). Unlabeled human rhabdomyosarcoma and lung adenocarcinoma cell lines, RD and A549, respectively, were a gift from Dragomira Majhen (Ruđer Bošković Institute, Zagreb, Croatia). Unlabeled human colorectal adenocarcinoma cell line, DLD-1, was a gift from Marin Barišić (Danish Cancer Institute, Copenhagen, Denmark). Unlabeled human high-grade serous ovarian cancer cell lines, OVKATE and OVSAHO, were purchased from Tebu-Bio. RPE-1, RD, A549, and DLD-1 cells were cultured in Dulbecco's Modified Eagle Medium (with 4.5 g/L D-glucose, stable glutamine, and sodium pyruvate; Capricorn Scientific), supplemented with 10% Fetal Bovine Serum (Sigma-Aldrich), 100 IU/mL penicillin, and 100 mg/mL streptomycin (Lonza). OVKATE and OVSAHO cell lines were cultured in RPMI 1640 medium (Sigma Aldrich) with the same supplements. Additionally, RPE-1 cells expressing EB3-GFP and H2B-mCherry were treated with 50 μg/mL of geneticin (Life Technologies). All cells were incubated at 37 °C in a Galaxy 170 R humidified incubator (Eppendorf) with a 5% CO_2 atmosphere. Routine *Mycoplasma* testing was performed by visually inspecting DAPI staining under the microscope. Passages were limited to a maximum of 8 to 10 wk (~10 passages). Cells were treated with a low dose of paclitaxel (taxol; National Cancer Institute), 2 h before live cell imaging or fixation. The concentration of 2 nM was chosen because it has been shown to reduce chromosome missegregation events in high-grade serous ovarian cancer and non–small cell lung carcinoma cells, while preserving the overall integrity of the spindle structure (15, 48).

Cell Transfection. The transfection of RPE-1 cell lines was carried out using the lipofection method. A day prior to siRNA transfection, 120,000 cells were seeded on 35-mm glass-bottom dishes with a glass thickness of 0.17 mm (ibidi GmbH). The siRNA constructs were diluted in Opti-MEM medium (Gibco), and transfection was performed with Lipofectamine RNAiMAX Reagent (Invitrogen) following the manufacturer's protocol. The constructs and their final concentrations used were as follows: 100 nM KIF18A siRNA (4390825; Ambion), 100 nM KIF4A siRNA (sc-60888; Santa Cruz Biotechnology), 20 nM HAUS8 siRNA (L-031247-01-0005; Dharmacon), and 100 nM NuMA siRNA (sc-43978; Santa Cruz Biotechnology). After a 4-h incubation with the transfection mixture, the medium was replaced with regular cell culture medium. All experiments involving siRNA-treated cells were conducted 24 h after transfection, except for HAUS8, where silencing was carried out for 48 h. The effectiveness of siRNA treatments was validated with immunostaining (*SI Appendix*, Fig. S1).

Cell Fixation and Immunostaining. In experiments aimed at determining anaphase errors and kinetochores-to-equator distances, cells were fixed in prewarmed 4% paraformaldehyde for 10 min. For assessing protein depletion by siRNA and PRC1-labeled overlap length, cells were fixed with ice-cold methanol for 1 min. Following fixation, cells were permeabilized for 15 min in 0.5% Triton X-100 in PBS. Subsequently, cells underwent blocking with 1% NGS in PBS for 1 h and were then incubated with primary antibodies overnight at 4 °C. Primary antibodies for siRNA-targeted genes of interest, PRC1, CREST, CENP-A, and tubulin were diluted at concentrations of 1:100, 1:100, 1:300, 1:300, and 1:500, respectively, in 1% NGS in PBS. After the primary antibody incubation, cells were incubated with fluorescence-conjugated secondary antibodies at room temperature for 1 h. Secondary antibodies for siRNA-targeted genes of interest, PRC1, CREST, CENP-A and tubulin were diluted at concentrations of 1:250, 1:250, 1:500, 1:500, and 1:1,000, respectively, in 2% NGS in PBS. Following each step, cells were washed three times in PBS for 5 min. The primary antibodies used were rabbit anti-KIF18A (A301-080A; Bethyl Laboratories), mouse anti-KIF4A (sc-365144; Santa Cruz Biotechnology), rabbit anti-HAUS8 (PA5-21331; Invitrogen), mouse anti-NuMA (sc-365532; Santa Cruz Biotechnology), mouse anti-PRC1 (sc-376983; Santa Cruz Biotechnology), rabbit anti-CENP-A (ab62242; Abcam), rat anti-alpha tubulin (MA1-80017, Invitrogen), and human anti-centromere protein antibody (Antibodies Incorporated). The secondary antibodies used were donkey anti-mouse IgG-Alexa Fluor 488 (Abcam), donkey anti-rabbit IgG-Alexa Fluor 488 (Abcam), donkey anti-mouse IgG-Alexa Fluor 594 (Abcam), donkey anti-rabbit IgG-Alexa 594 (Abcam), donkey anti-mouse IgG-Alexa Fluor 647 (Abcam), donkey anti-rat IgG-Alexa Fluor 594 (Abcam), donkey anti-rat IgG-Alexa Fluor 647 (Abcam), and goat anti-human IgG H&L DyLight 594 (Abcam). Additionally, DAPI (1 μg/mL) was added and incubated for 15 min at room temperature to visualize chromosomes.

Imaging of Fixed Cells. Immunostained cells, used to determine the effectiveness of siRNA treatments and PRC1-labeled overlap length, were imaged using the Bruker Opterra Multipoint Scanning Confocal Microscope (Bruker Nano Surfaces) and the Zeiss LSM 800 confocal microscope (Zeiss). The Opterra Multipoint Scanning Confocal Microscope (Bruker Nano Surfaces) was mounted on a Nikon Ti-E inverted microscope equipped with a Nikon CFI Plan Apo VC 100x/1.4 numerical aperture oil objective (Nikon). The system was controlled with Prairie View Imaging Software (Bruker). Images were captured with an Evolve 512 Delta EMCCD Camera (Photometrics). A 2x relay lens was placed in front of the camera, which resulted in the xy-pixel size in the image of 83 nm. Opterra Dichroic and Barrier Filter Set 405/488/561/640 was used to separate the excitation light from the emitted fluorescence with the following emission filters: BL HC 525/30, BL HC 600/37, and BL HC 673/11 (Semrock). The imaging was done on 5 central z-planes with 0.5-μm spacing. The Zeiss LSM 800 confocal microscope, with an Airyscan Superresolution Module and Axio Observer.Z1 inverted stand (Carl Zeiss

GmbH), was also used for imaging tubulin-immunostained cells and observing anaphase chromosome segregation errors. Only bipolar spindles were imaged, and they were imaged using multiple z-planes to encompass the entire anaphase spindle with all chromosomes. For excitation of blue, green, red, and far-red fluorescence, 405/488/561/640 laser lines were used, respectively. Images were captured using the LSM 800 camera with Plan-Apochromat 63x/1.40 Oil DIC M27 objective (Carl Zeiss GmbH) or Plan-Apochromat 40x/0.95 Corr M27 objective. The acquisition of interphase cells for micronuclei detection was conducted on fixed cells using the Zeiss LSM 800 confocal microscope with 40x/0.95 Corr M27 objective and Tiles recording mode on multiple z-planes to encompass the entire cell volume. The system was operated with ZEN blue 3.4 system software (Carl Zeiss GmbH).

Speckle Microscopy. Cells cultured on glass-bottom dishes were treated with 1 nM SiR-tubulin dye (Spirochrome AG). Following a 15-min staining, confocal live imaging was conducted using a Dragonfly spinning disk confocal microscope system (Andor Technology) equipped with a 63x/1.49 HC PL APO oil objective (Leica) and Sona 4.2P scientific complementary metal oxide semiconductor camera (Andor Technology), or an Expert Line easy3D STED microscope system (Abberior Instruments) with a 60x/1.2 UPLSAPO 60XW water objective (Olympus) and avalanche photodiode detector. Fusion software and Imspector software were utilized for image acquisition, respectively. Throughout the imaging process, cells were maintained at a temperature of 37 °C and a 5% CO_2 atmosphere within a heating chamber (Okolab). For live imaging of RPE-1 cells expressing CENP-A-GFP and centrin1-GFP, and dyed with SiR-tubulin, the Dragonfly microscope system utilized 488-nm and 640-nm laser lines for the excitation of GFP and SiR, respectively. Similarly, the Expert Line microscope system utilized 485-nm and 640-nm laser lines for the excitation of GFP and SiR, respectively. To visualize SiR-tubulin speckles, images were acquired with 80% laser power and an exposure time of 1 s. Image acquisition was performed on one or two focal planes every 5 or 10 s. To visualize the dynamics of speckles in the OVKATE and OVSAHO cell lines, SPY555-DNA dye (Spirochrome AG) was used to stain cell DNA at a final concentration of 100 nM, 2 h before imaging. To prevent dye efflux, a broad-spectrum efflux pump inhibitor, verapamil (Spirochrome AG), was introduced at a final concentration of 0.5 μM along with the DNA dye. Once the dye permeated the cells and metaphase spindles became discernible, 1 nM SiR-tubulin dye was introduced to visualize the dynamics of tubulin speckles. The imaging of speckles and DNA was conducted using 561-nm and 640-nm laser lines on the Dragonfly microscope system. To minimize potential side effects of SiR-tubulin and preserve the resolution of speckles on the microtubules, cells were not imaged more than 45 min after dye addition.

Imaging of EB3 Spots. The velocity of EB3 spots on astral microtubules was assessed in RPE-1 cells stably expressing EB3-GFP and H2B-mCherry. Metaphase cells were imaged every 2 s in a single z-plane for 1 min using the Dragonfly spinning disk confocal microscope system (Andor Technology). Image acquisition was operated with Fusion software (Andor Technology). Throughout the imaging process, cells were maintained at a temperature of 37 °C and a 5% CO_2 atmosphere within a heating chamber (Okolab). For excitation, 488-nm and 561-nm laser lines were used for visualization of GFP, and mCherry, respectively. A single central spindle z-plane, where both centrosomes were visible, was imaged with both laser lines every 2 s.

Image and Data Analysis. Image analysis and measurements were performed in Fiji/ImageJ (NIH). Quantification and data analysis were performed in R (R Foundation for Statistical Computing) and MATLAB (MathWorks). Figures and schemes were assembled in Adobe Illustrator CC (Adobe Systems). Statistical analysis was performed using Student's *t* test, Mann–Whitney test, and two-proportions z-test.

Protein depletion by siRNA was assessed by using immunofluorescence images, which allow for evaluation of protein levels at the relevant location (spindle) and phase (metaphase) in typical cells. The mean signal intensity within the spindle area was calculated and the background cytoplasm intensity measured in a 30 × 30 pixel region was subtracted. For siKIF18A+siNuMA treatment, NuMA signal was additionally measured only in the midzone of the metaphase spindle, to assess the change in the level of the subpopulation of NuMA that cross-links kinetochore and bridging microtubules. This was achieved by encompassing the area where kinetochores are located, measuring the mean signal of that area, and then subtracting the background cytoplasm intensity.

Anaphase chromosome errors were quantified by examining fixed RPE-1 anaphase cells with stable expression of CENP-A-GFP and centrin1-GFP, which were subsequently stained for tubulin and DNA. In the case of unlabeled cancer cells, fixation was followed by staining for tubulin, DNA, and CREST. Analysis was restricted to bipolar spindles, involving the inspection of multiple z-planes of spindles during anaphase. A chromosome was categorized as "lagging" if it trailed the dividing chromosome mass by at least 2 μm. If there was no gap in the DNA signal between two chromosome arms, these chromosomes were classified as chromosome bridges and excluded from the calculation. Only spindles not in contact with the telophase contractile ring were included in the analysis.

To quantify interphase micronuclei, images of fixed cells were examined in the DNA channel. The Multi-point tool was utilized to mark each cell nucleus and determine the total cell count in the image. All slices in the z-stack were inspected for micronuclei, and the occurrence of at least one micronucleus in a cell was documented. The tubulin channel was additionally inspected to confirm whether two or more micronuclei were associated with a single cell or multiple cells.

To measure kinetochore alignment on the spindle, we used the Multi-point tool to track the positions of sister kinetochore pairs. For RPE-1 cells, the measurements were obtained from live imaging, whereas the position of kinetochores in cancer cell lines was determined postimmunolabeling with the CREST antibody. The equatorial plane was defined as the line passing through two points positioned between the outermost pairs of kinetochores on opposite sides of the spindle. Chromosome alignment was then calculated as the distance between the midpoint of sister kinetochore pairs and the equatorial plane. Note that sister kinetochore pairs located near the centrosomes were excluded from consideration to prevent the tracking of kinetochores that are not in a bioriented configuration. Furthermore, the interkinetochore distance was determined by measuring the distance between tracked pairs of sister kinetochores.

To assess the antiparallel overlap length in cells immunostained for PRC1, a five-pixel-thick segmented line was used to trace the pole-to-pole contour within individual PRC1-labeled overlap regions. The pole-to-pole tracking was performed on single z-planes, and the mean value of the cytoplasmic intensity was subtracted from the obtained intensity profiles. The overlap length of individual PRC1-labeled regions was defined as the width of the intensity peak at the central part of the contour in SciDavis (Free Software Foundation Inc.). The width measurement was taken at the base of the PRC1 intensity peak, where the PRC1 signal roughly equals the mean value of the PRC1 signal along the contour on either side of the peak.

To assess microtubule poleward flux velocity using the speckle microscopy assay, we considered tubulin speckles that could be tracked for at least 30 s within the spindle. For each tubulin speckle position in RPE-1 cells, corresponding CENP-A and centrin positions, indicative of sister kinetochores and spindle poles, respectively, were tracked using the Multi-point tool. Speckles originating at a proximal kinetochore and associated with its proximal pole were categorized as part of the k-fiber, while those starting between sister kinetochores or proximal to the distal pole and passing through sister kinetochores were classified as part of the bridging fiber. In unlabeled cancer cell lines where kinetochores were not visible during live imaging, only the positions of speckles and spindle poles were tracked over time. Speckle-pole velocity was determined by fitting linear regression to the distances between the SiR-tubulin speckle and the associated spindle pole during the first 30 s of its trajectory. From the corresponding speckle trajectories, kinetochore positions were used to calculate kinetochore velocity. This was achieved by fitting a linear regression to the distances between kinetochores and the pole over the 30-s timeframe. The kinetochore was categorized as "leading" if it moved toward its associated pole and "trailing" if it moved away from its associated pole throughout the 30-s speckle trajectory. To ensure that kinetochores were actively leading or trailing, without being in a pausing state, a threshold was set. Kinetochores were selected based on a movement criterion within 10 s of at least 300 nm toward or away from the pole for leading and trailing kinetochores, respectively. The speckle–kinetochore velocity was then determined by fitting linear regression to the distances between the speckle and the associated kinetochore over the 30-s period.

EB3 velocity of astral microtubules was assessed in RPE-1 cells expressing EB3-GFP and H2B-mCherry. The positioning of chromosomes within the spindle was imaged to identify metaphase spindles. The trajectories of EB3 spots on astral

microtubules were acquired on a single z-plane using the Multipoint tool. In the same manner, EB3 spots within the spindle that terminate at chromosomes were tracked and used as indicators of the growing k-fiber microtubules. Tracking of the spots and their corresponding spindle poles was conducted over time, starting from the initial appearance of the spot to the last frame where the spot remained clearly visible. The tracking spanned at least 4 time points (8 s), and the spot velocity was determined by fitting linear regression to the spot-pole distances over time. Kymographs for EB3 spots were generated using a 10-pixel thick Straight Line, drawn from pole to pole, and then applying the KymographBuilder plugin.

Data, Materials, and Software Availability. All study data are included in the article and/or supporting information.

ACKNOWLEDGMENTS. We thank Alexey Khodjakov (New York State Department of Health), Patrick Meraldi (University of Geneva), Marin Barišić (Danish Cancer Institute), and Dragomira Majhen (Ruđer Bošković Institute) for cell lines, Anamaria Brozović (Ruđer Bošković Institute) for chemicals, and Ivana Šarić (Ruđer Bošković Institute) for the drawings. The Tolić lab is funded by the European Research Council (ERC Synergy Grant, GA Number 855158), the Croatian Science Foundation (HRZZ) through Swiss-Croatian Bilateral Projects (project IPCH-2022-10-9344), and projects cofinanced by the Croatian Government and the European Union through the European Regional Development Fund–the Competitiveness and Cohesion Operational Programme: IPSted (Grant KK.01.1.1.04.0057) and QuantiXLie Center of Excellence (Grant KK.01.1.1.01.0004).

Author affiliations: [a]Laboratory of Cell Biophysics, Division of Molecular Biology, Ruđer Bošković Institute, Zagreb 10000, Croatia

1. H. Maiato, A. Gomes, F. Sousa, M. Barisic, Mechanisms of chromosome congression during mitosis. *Biology* **6**, 13 (2017).
2. C. L. Fonseca *et al.*, Mitotic chromosome alignment ensures mitotic fidelity by promoting interchromosomal compaction during anaphase. *J. Cell Biol.* **218**, 1148–1163 (2019).
3. A. M. Gomes *et al.*, Micronuclei from misaligned chromosomes that satisfy the spindle assembly checkpoint in cancer cells. *Curr. Biol.* **32**, 4240–4254.e5 (2022).
4. C. Marquis *et al.*, Chromosomally unstable tumor cells specifically require KIF18A for proliferation. *Nat. Commun.* **12**, 1213 (2021).
5. R. J. Quinton *et al.*, Whole-genome doubling confers unique genetic vulnerabilities on tumour cells. *Nature* **590**, 492–497 (2021).
6. J. B. Tucker *et al.*, Misaligned chromosomes are a major source of chromosomal instability in breast cancer. *Cancer Res. Commun.* **3**, 54–65 (2023).
7. C.-Z. Zhang *et al.*, Chromothripsis from DNA damage in micronuclei. *Nature* **522**, 179–184 (2015).
8. S. Liu *et al.*, Nuclear envelope assembly defects link mitotic errors to chromothripsis. *Nature* **561**, 551–555 (2018).
9. I. Cortés-Ciriano *et al.*, Comprehensive analysis of chromothripsis in 2,658 human cancers using whole-genome sequencing. *Nat. Genet.* **52**, 331–341 (2020).
10. S. L. Thompson, S. F. Bakhoum, D. A. Compton, Mechanisms of chromosomal instability. *Curr. Biol.* **20**, R285–R295 (2010).
11. D. J. Gordon, B. Resio, D. Pellman, Causes and consequences of aneuploidy in cancer. *Nat. Rev. Genet.* **13**, 189–203 (2012).
12. K. Rowald *et al.*, Negative selection and chromosome instability induced by Mad2 overexpression delay breast cancer but facilitate oncogene-independent outgrowth. *Cell Rep.* **15**, 2679–2691 (2016).
13. P. Risteski, M. Jagrić, N. Pavin, I. M. Tolić, Biomechanics of chromosome alignment at the spindle midplane. *Curr. Biol.* **31**, R574–R585 (2021).
14. N. Ertych *et al.*, Increased microtubule assembly rates influence chromosomal instability in colorectal cancer cells. *Nat. Cell Biol.* **16**, 779–791 (2014).
15. N. Tamura *et al.*, Specific mechanisms of chromosomal instability indicate therapeutic sensitivities in high-grade serous ovarian carcinoma. *Cancer Res.* **80**, 4946–4959 (2020).
16. S. F. Bakhoum, G. Genovese, D. A. Compton, Deviant kinetochore microtubule dynamics underlie chromosomal instability. *Curr. Biol.* **19**, 1937–1942 (2009).
17. Y. Du, C. A. English, R. Ohi, The kinesin-8 Kif18A dampens microtubule plus-end dynamics. *Curr. Biol.* **20**, 374–380 (2010).
18. J. Stumpff, M. Wagenbach, A. Franck, C. L. Asbury, L. Wordeman, Kif18A and chromokinesins confine centromere movements via microtubule growth suppression and spatial control of kinetochore tension. *Dev. Cell* **22**, 1017–1029 (2012).
19. J. Stumpff, G. von Dassow, M. Wagenbach, C. Asbury, L. Wordeman, The kinesin-8 motor Kif18A suppresses kinetochore movements to control mitotic chromosome alignment. *Dev. Cell* **14**, 252–262 (2008).
20. Y. Cohen-Sharir *et al.*, Aneuploidy renders cancer cells vulnerable to mitotic checkpoint inhibition. *Nature* **590**, 486–491 (2021).
21. G. J. P. L. Kops, D. R. Foltz, D. W. Cleveland, Lethality to human cancer cells through massive chromosome loss by inhibition of the mitotic checkpoint. *Proc. Natl. Acad. Sci. U.S.A.* **101**, 8699–8704 (2004).
22. A. Janssen, G. J. P. L. Kops, R. H. Medema, Elevating the frequency of chromosome mis-segregation as a strategy to kill tumor cells. *Proc. Natl. Acad. Sci. U.S.A.* **106**, 19108–19113 (2009).
23. A. D. Silk *et al.*, Chromosome missegregation rate predicts whether aneuploidy will promote or suppress tumors. *Proc. Natl. Acad. Sci. U.S.A.* **110**, E4134–E4141 (2013).
24. L. M. Zasadil *et al.*, High rates of chromosome missegregation suppress tumor progression but do not inhibit tumor initiation. *Mol. Biol. Cell* **27**, 1981–1989 (2016).
25. M. Jagrić, P. Risteski, J. Martinčić, A. Milas, I. M. Tolić, Optogenetic control of PRC1 reveals its role in chromosome alignment on the spindle by overlap length-dependent forces. *eLife* **10**, e61170 (2021).
26. P. Risteski *et al.*, Length-dependent poleward flux of sister kinetochore fibers promotes chromosome alignment. *Cell Rep.* **40**, 111169 (2022).
27. J. Kajtez *et al.*, Overlap microtubules link sister k-fibres and balance the forces on bi-oriented kinetochores. *Nat. Commun.* **7**, 10298 (2016).
28. N. Pavin, I. M. Tolić, Mechanobiology of the mitotic spindle. *Dev. Cell* **56**, 192–201 (2021).
29. I. M. Tolić, Mitotic spindle: Kinetochore fibers hold on tight to interpolar bundles. *Eur. Biophys. J.* **47**, 191–203 (2018).
30. A. Forer, Local reduction of spindle fiber birefringence in living Nephrotoma suturalis (Loew) spermatocytes induced by ultraviolet microbeam irradiation. *J. Cell Biol.* **25**, 95–117 (1965).
31. Y. Hamaguchi, M. Toriyama, H. Sakai, Y. Hiramoto, Redistribution of fluorescently labeled tubulin in the mitotic apparatus of sand dollar eggs and the effects of taxol. *Cell Struct. Funct.* **12**, 43–52 (1987).
32. Y. Hiramoto, K. Izutsu, Poleward movement of "markers" existing in mitotic spindles of grasshopper spermatocytes. *Cell Struct. Funct.* **2**, 257–259 (1977).
33. T. J. Mitchison, Polewards microtubule flux in the mitotic spindle: Evidence from photoactivation of fluorescence. *J. Cell Biol.* **109**, 637–652 (1989).
34. A. C. Almeida *et al.*, Augmin-dependent microtubule self-organization drives kinetochore fiber maturation in mammals. *Cell Rep.* **39**, 110610 (2022).
35. V. Štimac, I. Koprivec, M. Manenica, J. Simunić, I. M. Tolić, Augmin prevents merotelic attachments by promoting proper arrangement of bridging and kinetochore fibers. *eLife* **11**, e83287 (2022).
36. Y. Steblyanko *et al.*, Microtubule poleward flux in human cells is driven by the coordinated action of four kinesins. *EMBO J.* **39**, e105432 (2020).
37. M. Sun *et al.*, NuMA regulates mitotic spindle assembly, structural dynamics and function via phase separation. *Nat. Commun.* **12**, 7157 (2021).
38. G. Goshima, M. Mayer, N. Zhang, N. Stuurman, R. D. Vale, Augmin: A protein complex required for centrosome-independent microtubule generation within the spindle. *J. Cell Biol.* **181**, 421–429 (2008).
39. T. Kamasaki *et al.*, Augmin-dependent microtubule nucleation at microtubule walls in the spindle. *J. Cell Biol.* **202**, 25–33 (2013).
40. G. Wu, R. Wei, E. Cheng, B. Ngo, W.-H. Lee, Hec1 contributes to mitotic centrosomal microtubule growth for proper spindle assembly through interaction with Hice1. *Mol. Biol. Cell* **20**, 4686–4695 (2009).
41. C. L. Hueschen, S. J. Kenny, K. Xu, S. Dumont, NuMA recruits dynein activity to microtubule minus-ends at mitosis. *eLife* **6**, e29328 (2017).
42. A. Merdes, K. Ramyar, J. D. Vechio, D. W. Cleveland, A complex of NuMA and cytoplasmic dynein is essential for mitotic spindle assembly. *Cell* **87**, 447–458 (1996).
43. C. Wandke *et al.*, Human chromokinesins promote chromosome congression and spindle microtubule dynamics during mitosis. *J. Cell Biol.* **198**, 847–863 (2012).
44. M. A. Garcia, N. Koonrugsa, T. Toda, Spindle–kinetochore attachment requires the combined action of Kin I-like Klp5/6 and Alp14/Dis1-MAPs in fission yeast. *EMBO J.* **21**, 6015–6024 (2002).
45. M. I. Mayr *et al.*, The human kinesin Kif18A is a motile microtubule depolymerase essential for chromosome congression. *Curr. Biol.* **17**, 488–498 (2007).
46. R. R. West, T. Malmstrom, J. R. McIntosh, Kinesins *klp5* + and *klp6* + are required for normal chromosome movement in mitosis *J. Cell Sci.* **115**, 931–940 (2002).
47. C. Zhu *et al.*, Functional analysis of human microtubule-based motor proteins, the kinesins and dyneins, in mitosis/cytokinesis using RNA interference. *Mol. Biol. Cell* **16**, 3187–3199 (2005).
48. E. A. Crowley, N. M. Hermance, C. P. Herlihy, A. L. Manning, Suppression of chromosome instability limits acquired drug resistance. *Mol. Cancer Ther.* **21**, 1583–1593 (2022).
49. S. L. Thompson, D. A. Compton, Chromosome missegregation in human cells arises through specific types of kinetochore–microtubule attachment errors. *Proc. Natl. Acad. Sci. U.S.A.* **108**, 17974–17978 (2011).
50. I. Matos *et al.*, Synchronizing chromosome segregation by flux-dependent force equalization at kinetochores. *J. Cell Biol.* **186**, 11–26 (2009).
51. P. Risteski, Permeable dye-based fluorescent speckle microscopy for human cells. *Nat. Rev. Mol. Cell Biol.* **24**, 308–308 (2023).
52. G. Lukinavičius *et al.*, Fluorogenic probes for live-cell imaging of the cytoskeleton. *Nat. Methods* **11**, 731–733 (2014).
53. J. D. Warren, B. Orr, D. A. Compton, "A comparative analysis of methods to measure kinetochore-microtubule attachment stability" in *Methods in Cell Biology*, (Elsevier, 2020), pp. 91–116.
54. B. Polak, P. Risteski, S. Lesjak, I. M. Tolić, PRC1-labeled microtubule bundles and kinetochore pairs show one-to-one association in metaphase. *EMBO Rep.* **18**, 217–230 (2017).
55. T. Stepanova *et al.*, Visualization of microtubule growth in cultured neurons via the use of EB3-GFP (end-binding protein 3-green fluorescent protein). *J. Neurosci.* **23**, 2655–2664 (2003).
56. A. C. Amaro *et al.*, Molecular control of kinetochore-microtubule dynamics and chromosome oscillations. *Nat. Cell Biol.* **12**, 319–329 (2010).
57. J. W. Armond, E. F. Harry, A. D. McAinsh, N. J. Burroughs, Inferring the forces controlling metaphase kinetochore oscillations by reverse engineering system dynamics. *PLOS Comput. Biol.* **11**, e1004607 (2015).
58. K. Jaqaman *et al.*, Kinetochore alignment within the metaphase plate is regulated by centromere stiffness and microtubule depolymerases. *J. Cell Biol.* **188**, 665–679 (2010).
59. S. Domcke, R. Sinha, D. A. Levine, C. Sander, N. Schultz, Evaluating cell lines as tumour models by comparison of genomic profiles. *Nat. Commun.* **4**, 2126 (2013).
60. B. M. Barnes *et al.*, Distinct transcriptional programs stratify ovarian cancer cell lines into the five major histological subtypes. *Genome Med.* **13**, 140 (2021).
61. E. Choi *et al.*, BRCA2 fine-tunes the spindle assembly checkpoint through reinforcement of BubR1 acetylation. *Dev. Cell* **22**, 295–308 (2012).
62. Å. Ehlén *et al.*, Proper chromosome alignment depends on BRCA2 phosphorylation by PLK1. *Nat. Commun.* **11**, 1819 (2020).

63. B. DepMap, DepMap 23Q4 Public. Figshare. https://doi.org/10.25452/FIGSHARE.PLUS.24667905.V2. Accessed 29 May 2024.
64. M. Ghandi *et al.*, Next-generation characterization of the Cancer Cell Line Encyclopedia. *Nature* **569**, 503–508 (2019).
65. A. Guerreiro *et al.*, WDR62 localizes katanin at spindle poles to ensure synchronous chromosome segregation. *J. Cell Biol.* **220**, e202007171 (2021).
66. N. J. Ganem, D. A. Compton, Functional roles of poleward microtubule flux during mitosis. *Cell Cycle* **5**, 481–485 (2006).
67. A. Mallavarapu, K. Sawin, T. Mitchison, A switch in microtubule dynamics at the onset of anaphase B in the mitotic spindle of Schizosaccharomyces pombe. *Curr. Biol.* **9**, 1423–1428 (1999).
68. P. S. Maddox, K. S. Bloom, E. D. Salmon, The polarity and dynamics of microtubule assembly in the budding yeast Saccharomyces cerevisiae. *Nat. Cell Biol.* **2**, 36–41 (2000).
69. M. K. Gardner *et al.*, Chromosome congression by kinesin-5 motor-mediated disassembly of longer kinetochore microtubules. *Cell* **135**, 894–906 (2008).
70. H. Mary *et al.*, Fission yeast Kinesin-8 controls chromosome congression independently of oscillations. *J. Cell Sci.* **128**, 3720–3730 (2015).
71. A. H. Klemm, A. Bosilj, M. Glunčić, N. Pavin, I. M. Tolić, Metaphase kinetochore movements are regulated by kinesin-8 motors and microtubule dynamic instability. *Mol. Biol. Cell* **29**, 1332–1345 (2018).
72. N. Ma *et al.*, Poleward transport of TPX2 in the mammalian mitotic spindle requires dynein, Eg5, and microtubule flux. *Mol. Biol. Cell* **21**, 979–988 (2010).
73. N. J. Ganem, K. Upton, D. A. Compton, Efficient mitosis in human cells lacking poleward microtubule flux. *Curr. Biol.* **15**, 1827–1832 (2005).
74. D. Dudka *et al.*, Complete microtubule–kinetochore occupancy favours the segregation of merotelic attachments. *Nat. Commun.* **9**, 2042 (2018).
75. K. Iemura, T. Natsume, K. Maehara, M. T. Kanemaki, K. Tanaka, Chromosome oscillation promotes Aurora A–dependent Hec1 phosphorylation and mitotic fidelity. *J. Cell Biol.* **220**, e202006116 (2021).
76. A. Warren *et al.*, Global computational alignment of tumor and cell line transcriptional profiles. *Nat. Commun.* **12**, 22 (2021).
77. A. Czechanski *et al.*, Kif18a is specifically required for mitotic progression during germ line development. *Dev. Biol.* **402**, 253–262 (2015).
78. L. A. Sepaniac *et al.*, Micronuclei in *Kif18a* mutant mice form stable micronuclear envelopes and do not promote tumorigenesis. *J. Cell Biol.* **220**, e202101165 (2021).
79. A. E. Mammel, H. Z. Huang, A. L. Gunn, E. Choo, E. M. Hatch, Chromosome length and gene density contribute to micronuclear membrane stability. *Life Sci. Alliance* **5**, e202101210 (2022).
80. S. J. Klaasen *et al.*, Nuclear chromosome locations dictate segregation error frequencies. *Nature* **607**, 604–609 (2022).
81. P. F. Cosper, S. E. Copeland, J. B. Tucker, B. A. Weaver, Chromosome missegregation as a modulator of radiation sensitivity. *Semin. Radiat. Oncol.* **32**, 54–63 (2022).
82. C. R. Gliech *et al.*, Weakened APC/C activity at mitotic exit drives cancer vulnerability to KIF18A inhibition. *EMBO J.* **43**, 666–694 (2024).
83. M. Payton *et al.*, Small-molecule inhibition of kinesin KIF18A reveals a mitotic vulnerability enriched in chromosomally unstable cancers. *Nat. Cancer* **5**, 66–84 (2023).